

Passive solar high-yield seawater desalination by modular and low-cost distillation

Eliodoro Chiavazzo ^{*}, Matteo Morciano , Francesca Viglino, Matteo Fasano  and Pietro Asinari ^{*}

Although seawater is abundant, desalination is energy intensive and expensive. Using the Sun as an energy source is attractive for desalinating seawater. Although interesting, current passive devices with no moving parts have unsatisfactory performance when operated with an energy flux lower than 1 kW m^{-2} (one sun). We present a passive multi-stage and low-cost solar distiller, where efficient energy management leads to significant enhancement in freshwater yield. Each unit stage for complete distillation is made of two hydrophilic layers separated by a hydrophobic microporous membrane, with no other mechanical ancillaries. Under realistic conditions, we demonstrate a distillate flow rate of almost $3\text{ l m}^{-2}\text{ h}^{-1}$ from seawater at less than one sun—twice the yield of recent passive complete distillation systems. Theoretical models also suggest that the concept has the potential to further double the observed distillate rate. In perspective, this system may help satisfy the freshwater needs in isolated and impoverished communities in a sustainable way.

Four billion people currently face severe water scarcity for at least one month per year, and half a billion face it all year round^{1–3}.

This widespread and devastating problem has motivated the development of a large variety of desalination technologies to provide freshwater from the abundant seawater, by means of either membranes or thermal processes. However, most of the systems involve costly or cumbersome solutions^{4–6}. Conventional desalination technologies are typically based on active processes; namely, they include components with mechanical moving parts that are subject to ageing and possible failure. Since active desalination involves high capital and operating costs, large plants are generally implemented.

In contrast, passive desalination technology is built using self-operating systems, where all processes occur without mechanical moving parts. Although usually less energy efficient compared to active technologies, passive approaches have the potential to improve the economic feasibility and reliability of small plants owing to their lower capital requirements and operating costs, especially in isolated and impoverished areas⁷. In particular, variations of solar stills have been used for thousands of years, and they have the major advantage that they operate using only the Sun. However, even their best realizations can be highly inefficient, and large-area installations are typically required to satisfy the drinkable water needs (for example, 2 l per day⁸) of a single person: 6 m^2 per person per day⁹.

In recent years, advanced nanomaterials have been used to improve the yield of stills by reducing heat losses to the environment and enhancing the solar energy absorption^{10–17}. Some efforts have been so successful that sunlight could be converted to steam and then condensed with efficiency in the order of 90%, even without optical concentration. Owing to such progress, an incredibly high quantity of completely distilled water produced by 1 kWh of input solar energy was achieved by a solar still made of inexpensive materials (1.28 l kWh^{-1} under one sun; that is, $1.28\text{ l m}^{-2}\text{ h}^{-1}$)¹⁸. This milestone can potentially increase the productivity of conventional solar stills by a factor of four, at the cost of a few dollars^{9,18–21}. Other strategies to further enhance the energy efficiency in solar steam generation have been reported recently, including superior light absorbance and additional energy gain from the

surroundings obtained through three-dimensional (3D) photo-thermal structures^{22–24}, and the reduced latent heat of water cluster evaporation claimed to be achieved in the molecular mesh of hierarchically nanostructured gels, which possibly leads to a small residual salt content in the condensate (partial distillation)²⁵. However, when condensing freshwater in a solar still, a large amount of latent energy is always lost to the environment. This occurs regardless of the level of sophistication of the nanomaterials used for evaporating saltwater (possibly only partially) and the thermal insulation of the liquid phase. Previous attempts to recover latent heat of condensation to enhance desalination performance intrinsically involved active components (for example, pumps), as in the case of vertical or inclined multi-effect solar stills^{26–28}, whereas attempts to recover it in a passive way were not supported by experimental evidence²⁹, possibly owing to distillate contamination issues.

Here, we design, build and test a completely passive solar-driven distiller capable of reusing the latent heat of vaporization several times before it is lost to the environment. This process is implemented in a completely passive way at ambient pressure, since the Sun provides thermal energy for complete distillation. Capillary forces, which can also be used by floating installations, drive water feeding. Furthermore, the latent heat of condensation of distillate is recovered by multiple complete evaporation/condensation stages, which allows the system to go beyond the thermodynamic limit of single-stage complete distillation $q_{\text{solar}}/\Delta h_{\text{LV}} = \sim 1.47\text{ l m}^{-2}\text{ h}^{-1}$ under one sun ($q_{\text{solar}} = 1\text{ kW m}^{-2}$), where $\Delta h_{\text{LV}} = 2,455.6\text{ kJ kg}^{-1}$ is the enthalpy of liquid–vapour complete-phase change at ambient temperature¹⁸. Although it is beyond the scope of the present work, this key concept possibly also applies to devices realizing only partial distillation²⁵, since it would still increase the purified water productivity. In our device, both passive water feeding and multi-stage complete distillation have been unlocked by the horizontal orientation of distillation stages. However, in contrast with previous attempts, the innovative use of a hydrophobic membrane between the evaporating and condensing hydrophilic layers helps avoid distillate contamination under horizontal configuration. We demonstrate, both experimentally and theoretically, that tremendous improvements in the distillate flow rate (two to four times greater

than state-of-the-art passive solar stills used for complete distillation¹⁸) can easily be achieved without compromising the simplicity and materials costs. For example, assuming the theoretical distillate flow rate reported in Supplementary Fig. 12 (namely, $\sim 6 \text{ l m}^{-2} \text{ h}^{-1}$), a single square metre of distiller exposed to direct solar radiation (for six working hours) theoretically has the potential to satisfy the daily drinkable water needs (2 litres per day²⁶) of up to 18 people. The reported approach and results represent a remarkable improvement over recently published passive technologies for complete distillation, and could possibly have an impact on the lives of millions of people in the most impoverished regions of the world³⁰.

Results

Layout of the passive solar distiller. Our modular distiller can passively desalinate seawater by exploiting low-temperature heat (here, from non-concentrated solar radiation) without the need for any mechanical or electrical ancillaries, such as pumps or valves, under standard operating conditions and by performing a complete distillation. The main elements are shown in Fig. 1a,b, while further technical details are available in Supplementary Figs. 1 and 2. Each stage of the distiller consists of two highly thermally conductive thin aluminium plates of $12 \times 12 \text{ cm}^2$, each supporting a 1-mm-thick layer of hydrophilic microfibre. The liquid layer separation can be accomplished using either hydrophobic microporous membranes, as is common in membrane distillation (for active technologies)^{31–33}, or a membrane-free solution with a small air gap between the hydrophilic layers. Both approaches are implemented and tested in this work. However, we note that the use of a hydrophobic membrane can be beneficial for avoiding accidental salt contamination of freshwater in the condensing layer, thus safely allowing realization of submillimetre air gaps and arbitrary orientation of the distiller. The materials used for the hydrophilic layer, rigid spacer and hydrophobic microporous membrane are reported in Supplementary Fig. 3a–c, respectively.

As depicted in Fig. 1a, solar radiation is absorbed and converted into heat on the upper side of the first stage of the distiller. TiNOX—a commercially available spectrally selective solar absorber³⁴—is used to increase the conversion efficiency of the solar radiation into heat, without any loss of generality with regards to the multi-stage concept. TiNOX shows high solar absorbance ($\alpha = 0.95$) and limited infrared emissivity ($\epsilon = 0.04$), and thus limited radiative loss at the same time. A transparent thermal insulating layer is adopted at the top surface to reduce convective heat loss between the spectrally selective solar absorber and ambient environment (see Supplementary Fig. 3d). This thermal insulator consists of three 2-mm-thick air layers, which are created between thin films of transparent linear low-density polyethylene (LLDPE) supported by an acrylonitrile butadiene styrene frame, manufactured by 3D printing. In these air layers, convective heat transfer is limited and, thus, mainly thermal conduction occurs. Finally, an aluminium heat sink is placed at the bottom of the distiller to efficiently reject heat from the last stage of the distiller to the ambient environment. It is worth stressing that, in this work, the heat sink purposely operates under natural convection and thus does not require any additional power supply. Note that the heat sink shape was not optimized and, therefore, further gains in efficiency can possibly follow from subsequent device design improvements.

Working principle of the distiller. The mechanism underpinning the desalination process of the N -stage distiller is based on reducing the characteristic distance separating the two thin hydrophilic layers, thus enabling an efficient, multiple, complete evaporation/condensation cycle at ambient pressure. In Fig. 1c, the distiller stage is depicted, where the evaporator and condenser are the upper and lower hydrophilic layers, respectively. These hydrophilic layers are mainly glued to the aluminium plates, apart from a protruding strip

that is immersed in either the saltwater (evaporator) or the distillate (condenser) basin. Water flux to and from the distiller relies only on capillary forces (owing to the hydrophilicity of the layers and inlet/outlet strips) and gravity, respectively.

Under operating conditions, saltwater rises to the upper hydrophilic layer in each stage (evaporator) because of capillarity. A thermal gradient is generated from the top to the bottom of the distiller by solar radiation absorption on the top surface. Therefore, in each stage, the upper aluminium plate heats the salty water in the evaporator, promoting vapour flux through the air gap or microporous membrane. As schematically represented in Fig. 1c, water in the evaporator and condenser has different vapour pressures because of the temperature and salinity gradients through the stage, which leads to a steady net vapour flux from the evaporating to condensing hydrophilic layers. In Fig. 1d, the vapour pressure is plotted as a function of water salinity and temperature, which helps illustrate the above process (see equations (1)–(3)). Water vapour condenses on each lower hydrophilic layer, where the released latent heat becomes available to drive additional evaporation stages in devices with a multi-stage configuration. The reuse of heat by subsequent stages is essential for overcoming the performance limitations of current passive distillers. As a result, completely distilled water accumulates in the hydrophilic condensation layer, and its strip drains the excess freshwater into the distillate basin (aided by gravity). It is worth pointing out that in contrast with traditional solar stills where the optical transmittance of the transparent cover may be reduced by condensed water drops, here the condensation process does not affect the optical performance of the device.

Laboratory experiments. The passive distiller was tested under both laboratory and outdoor conditions. First, the performance was assessed under laboratory conditions, where a non-fluctuating thermal source from an electrical resistor was adopted to ensure a constant thermal gradient (Fig. 2b and Supplementary Fig. 4). The distiller prototype was evaluated by the test rig depicted in Supplementary Fig. 5. In the laboratory, we evaluated distillers with different numbers of stages (1, 3 or 10 stages) and various condensing–evaporating interface layers (membrane-free, 0.1 or 3.0 μm polytetrafluoroethylene (PTFE) membranes). The feed water processed in these experiments was a water/NaCl solution that mimics the salinity of seawater at 35 g l^{-1} . The distillate fluxes measured for these different distiller configurations are presented in Fig. 2a, Supplementary Table 1 and Supplementary Note 1.

Experimental results in Fig. 2a show that the three-stage configuration device gave a threefold increase in the specific mass flow rate with respect to a one-stage configuration, and this already goes beyond the thermodynamic theoretical limit of single-stage distillers. Additionally, a sixfold increase relative to a one-stage configuration was observed using the ten-stage configuration. In particular, the configuration with 0.1 μm PTFE membranes and 10 stages produced a specific mass flow rate (J) of $2.95 \pm 0.02 \text{ l m}^{-2} \text{ h}^{-1}$ distillate with salinity $< 0.01 \text{ g l}^{-1}$ (resolution of the refractometer), which corresponds to $3.28 \pm 0.04 \text{ kWh}^{-1}$ and is a 2.5-fold enhancement with respect to state-of-the-art passive solar desalination systems for complete distillation¹⁸. The experimental distillate flow rates of the passive distillers fall within the error range of theoretical predictions (grey band in Fig. 2a; see Methods for details on the theoretical model). Moreover, the distillate flux obtained experimentally for a 1-stage configuration has been interpreted by a 3D finite element model of the setup (discrepancy less than 10%), to quantify the impact of each thermal loss channel (see Supplementary Note 2 and Supplementary Figs. 6 and 7).

The nonlinear relationship between the number of stages and distillate specific mass flow rate enhancement is due to a reduced temperature difference across each stage, which is gradually less effective at counteracting the vapour pressure gradient imposed

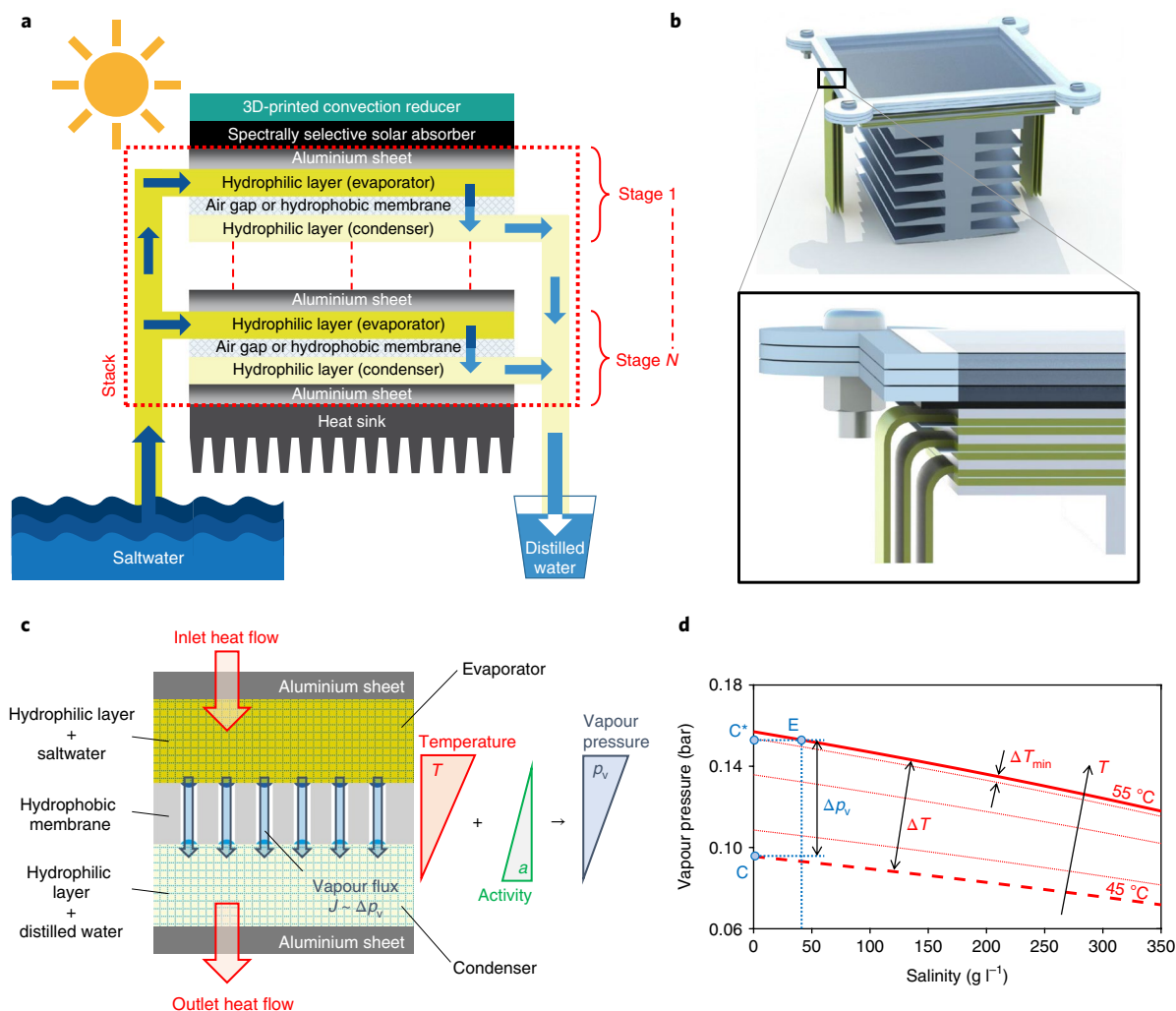


Fig. 1 | Layout of the solar passive distiller during day hours. **a**, Schematic of the modular distiller. First, seawater is provided to the device by capillary action through strips protruding from the hydrophilic layers of each stage. Second, solar radiation is converted into thermal energy by a spectrally selective material and then employed to drive multiple evaporation and condensation stages through either air gaps or hydrophobic membranes. Finally, distilled water is collected in a basin by gravity force. A 3D-printed transparent insulator (top) and aluminium heat sink (bottom) were adopted to reduce and enhance convective heat transfer, respectively. Red dashed and dotted lines enclose the N -stages of the distiller; dark and light blue arrows represent saltwater and distilled water flows, respectively. **b**, Isometric view (top) and section detail (bottom) of the three-stage solar desalination prototype (see also Supplementary Fig. 1). During experiments, input and output strips were not directly exposed to air: each strip was covered by an LLDPE film to suppress natural evaporation. **c**, Single stage of the distiller: the vapour flux from the evaporation (saltwater) to condensation (distillate) layer is proportional to the vapour pressure gradient through the stage, which results from the competing effects of temperature and activity (that is, salinity) gradients through the hydrophobic membrane. **d**, Vapour pressure versus water salinity and temperature, where the red lines are isothermal curves. The red solid and dashed lines are isothermal curves of the evaporator (55 °C) and condenser (45 °C) in the one-stage distiller reported in Supplementary Fig. 4a, respectively. During operations, the temperature gradient (in this schematic, represented neglecting the thermal resistances of hydrophilic layers and air) $\Delta T = 10$ °C induces a vapour pressure gradient Δp_v between the evaporator (point E; saltwater with 35 g l⁻¹) and condenser (point C; distillate with 0 g l⁻¹), and thus a net vapour flux. Point C* represents the state of the condensing layer with the minimum temperature gradient ΔT_{\min} to carry out water distillation.

by the salinity (see Fig. 1c,d for a graphical representation of this effect). It is interesting to note that devices with either air gaps or hydrophobic membranes show similar performance. In fact, while the ~1-mm-thick air gap guarantees a larger temperature gradient at the evaporator–condenser interface because of a lower thermal transmittance (air gap transmittance: ~100 W m⁻²K⁻¹; membrane average transmittance: ~470 W m⁻²K⁻¹), the permeability coefficient is reduced because of the larger gap thickness (air gap permeability: ~8 × 10⁻⁸ kg m⁻² Pa⁻¹ s⁻¹; membrane average permeability ~6 × 10⁻⁷ kg m⁻² Pa⁻¹ s⁻¹). This balance between the different heat and mass transfer characteristics of the two solutions results in their similar performances.

Field experiments. Next, we performed experimental tests of the three- and ten-stage configurations of the distiller under outdoor conditions. The passive distiller was first tested on a rooftop in Torino, Italy. The experimental setup adopted for the outdoor tests is pictured in Supplementary Fig. 8. Outdoor measurements were carried out on clear days around 12:00, when an approximately constant level of solar irradiance, $q_{\text{solar}} = \sim 600$ W m⁻², was achieved for at least four consecutive hours (see Fig. 2d and Supplementary Fig. 9). Seawater collected from the Ligurian Sea, with a salinity of 35 g l⁻¹, was supplied to the distiller to better match field-testing conditions. When exposed to direct sunlight, the 10-stage distiller achieved 2.07 ± 0.11 kWh⁻¹ distillate productivity, which is above

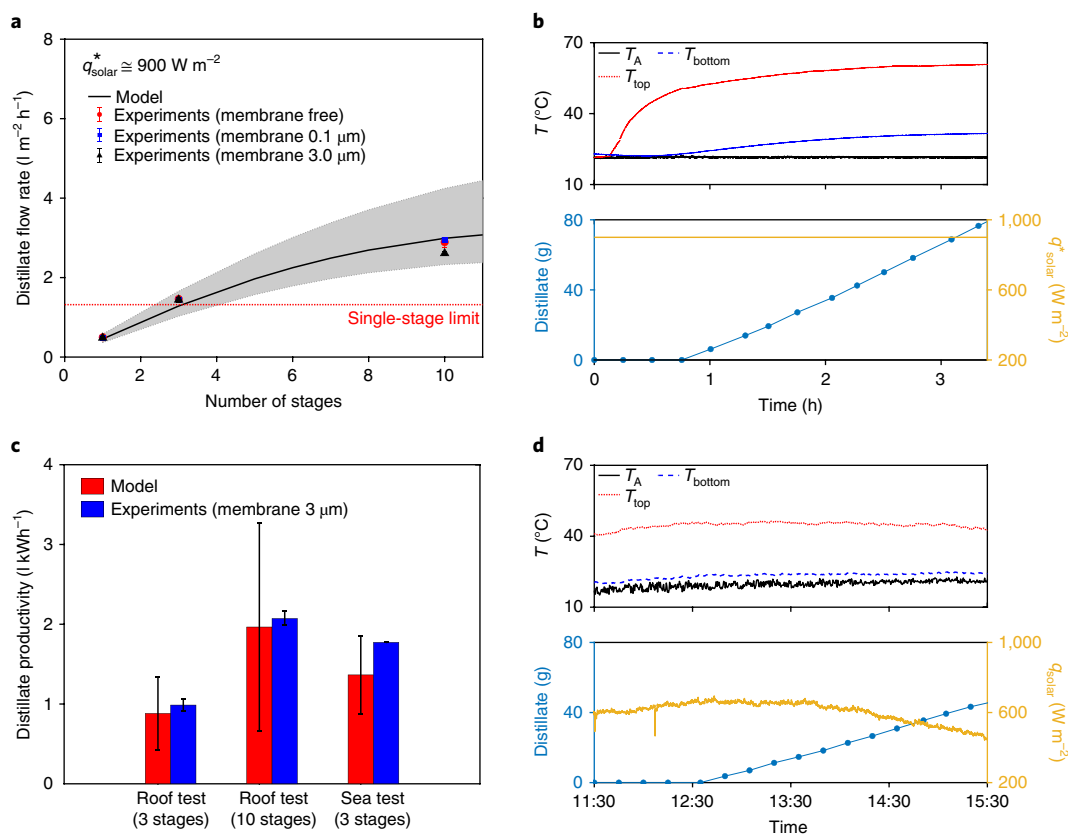


Fig. 2 | Desalination performance of the modular distiller. **a**, The desalination performance of the distiller was tested under laboratory conditions, with 740 W m^{-2} input thermal energy (about $q_{\text{solar}}^* = 900 \text{ W m}^{-2}$ equivalent solar irradiance, which includes the solar transmittance of the thermal insulator τ and the solar absorbance of the selective solar absorber α) and different numbers of stages. The distiller was tested with different interface configurations between the evaporation and condensation layers: membrane free, and hydrophobic membranes with pore sizes of 0.1 or $3.0 \mu\text{m}$. The model prediction and uncertainty for the membrane with a $3.0 \mu\text{m}$ pore size are represented by the black line and grey band, respectively. The red dotted line represents the thermodynamic theoretical limit of single-stage distillers under 900 W m^{-2} ($1.321 \text{ l m}^{-2} \text{ h}^{-1}$) for complete distillation. See Supplementary Note 1 for details. **b**, Temperature profiles, distillate production and equivalent solar irradiance during laboratory testing of the 10-stage distiller ($3.0 \mu\text{m}$ membrane). Solid black, dotted red and dashed blue lines represent the ambient (T_A), top, first-stage evaporator (T_{top}) and bottom, last-stage condenser temperatures (T_{bottom}), respectively. Distillate productivity was computed at steady-state conditions. **c**, Theoretical and experimental desalination performances of distillers with different numbers of stages, under outdoor conditions. The distillate productivity indicates the litres of distilled water produced per kWh of solar energy input. Roof and sea tests refer to the configurations in Supplementary Figs. 8 and 10, respectively. **d**, Temperature profiles, distillate production and solar irradiance during the outdoor roof test (Torino, Italy) of the 10-stage distiller. The legend is the same as in **b**. The average distillate flow rate and its uncertainty were computed in the interval from approximately 13:30 to 15:30. All error bars represent $\pm 1 \text{ s.d.}$

the thermodynamic limit of single-stage solar stills. In Fig. 2c and Supplementary Table 1, these distillate fluxes are reported in terms of litres of distilled water produced per kWh of solar energy input, for better comparability between different ambient conditions. The good performance of the distillers in the laboratory was maintained during outdoor tests. By considering outdoor boundary conditions (see Supplementary Table 2), the rooftop performances of the passive distiller are also within the calculated uncertainties of the theoretical model.

A floating configuration of the three-stage passive distiller was then tested in the sea. The distiller, when positioned on a floating platform above the sea, is able to pick up seawater, desalinate it by a distillation process that exploits only incoming solar energy and deliver a steady flux of freshwater into a storage basin (see Supplementary Fig. 10). The test was carried out on a clear day from 12:00 for 4 h; the solar irradiation was monitored and is depicted in Supplementary Fig. 11 (846 W m^{-2} on average), and the inlet seawater had a salinity of 35 g l^{-1} . Under these conditions, the floating distiller showed about 1.771 kWh^{-1} distillate productivity with a salinity $< 0.01 \text{ g l}^{-1}$, which is again above the thermodynamic limit

of single-stage solar stills for complete distillation and is in good accordance with modelling predictions (see Fig. 2c).

Since the experimental results matched well with predictions from the theoretical modelling, the model was then used to predict the potential specific mass flux of distillate as a function of the number of stages and salinity (see Supplementary Fig. 12). We note that the total temperature drop across the distiller might be further increased by optimizing the layered structure of each stage (see Supplementary Note 3). In these cases, the distiller has the potential to achieve a specific mass flux of distillate up to $61 \text{ m}^{-2} \text{ h}^{-1}$ under 900 W m^{-2} (namely, $\sim 6.661 \text{ kWh}^{-1}$), and even to efficiently process feed water with high salinity (for example, brines).

Salt removal. During day hours, the solar-driven distillation process leads to salt accumulation in the hydrophilic layers used as evaporators. This increase in salt concentration progressively reduces the productivity of each distillation stage because of the lower activity of high-salinity solutions (see equations (1) and (2)). The salinity gradient tends to vanish during night hours, when distillate production is interrupted while the high-salinity water in the evaporator

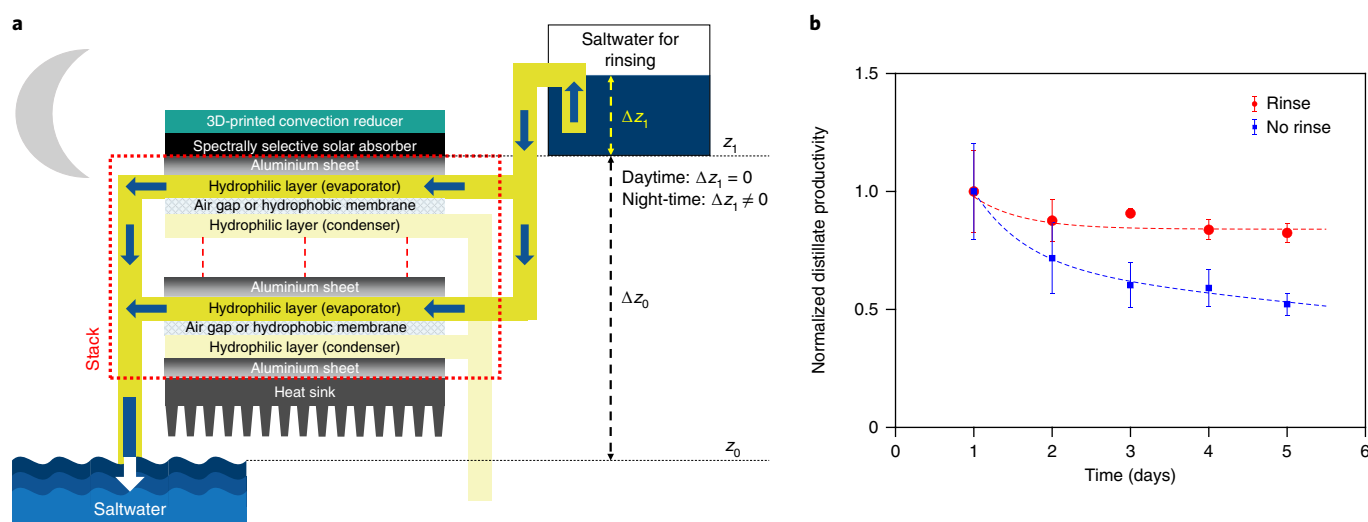


Fig. 3 | Salt removal and durability of desalination performance during night hours. **a**, The solar-driven distiller operates during day hours, progressively increasing the salt concentration in the evaporating layers. During night hours, instead, the salt accumulated in the evaporators diffuses back into the saltwater basin due to the concentration gradient and gravity. This salt removal process can be improved by rinsing the hydrophilic layers of the evaporators with a saltwater flow driven by the hydraulic head (Δz_1). **b**, Durability of desalination performance in a three-stage distiller under laboratory conditions. The distillate productivity measured each day (1 kWh^{-1}) was normalized by the value obtained on the first day of the experiments, when a new prototype was tested. Day (distillate production, salt accumulation) and night (no distillate production, salt removal) operations were considered for five consecutive days. Two alternative configurations are compared for the night operations: salt removal by concentration gradient and gravity (blue squares); and salt removal assisted by saltwater rinse (red dots). The red and blue lines are guides for the eyes. Error bars represent $\pm 1 \text{ s.d.}$

can diffuse back into the saltwater source (for example, the sea). This salt removal process is also aided by gravity because of the different density of high- and low-salinity solutions. However, based on our experience, such passive salt removal from the evaporator is a slow phenomenon occurring on longer time scales compared with the available night hours. Therefore, we now describe one possible engineering solution to this problem. The salt evacuation rate given by these passive processes could be enhanced by rinsing the hydrophilic layers with an additional flow of seawater (for example, with 35 g l^{-1} salinity). In the configuration detailed in Fig. 3a, the hydrophilic layers where evaporation occurs are connected to a rinse basin via additional hydrophilic strips. The rinse basin is empty during day hours ($\Delta z_1 = 0 \text{ cm}$, see Fig. 3a), whereas it is filled up with seawater during night hours. The resulting small hydraulic head ($\Delta z_1 = \sim 1 \text{ cm}$) drives the rinse of evaporating layers.

To assess the salt removal effectiveness of the rinse, the average distillate productivity of a three-stage distiller was monitored under laboratory conditions over five consecutive days. Each day, the distiller was powered for eight consecutive hours by a non-fluctuating thermal source (approximately equivalent to one sun irradiation) to maintain stable distillate production. Since each stage generated approximately 50 ml of distilled water over 8 h, $\sim 1.75 \text{ g}$ of salt accumulated in each evaporating layer. At this point, two alternative strategies were possible: salt removal by concentration gradient and gravity (without rinse); or salt removal assisted by saltwater rinse (with rinse; see Fig. 3a). In the strategy with rinse, each evaporating layer was also connected to the rinse basin through the additional hydrophilic strip. Each evaporating layer was rinsed for 1 min with a saltwater (35 g l^{-1}) flow of 0.8 ml s^{-1} , which resulted overall in 150 ml of saltwater per rinse. In both strategies, during the remaining 16 h, the produced distilled water was removed from the distillate basin, while the strips of the three evaporators were kept immersed in the saltwater basin (35 g l^{-1} salinity), relying on salt diffusion.

The distillate productivity measured each day was normalized by the value obtained on the first day of the experiments, when a new prototype was tested. In Fig. 3b, the two alternative configura-

tions are compared: salt removal without rinse (blue squares); and salt removal assisted by saltwater rinse (red dots). The distillate productivity obtained without rinse showed a significant decay with time, due to progressive salt accumulation in the hydrophilic layer of the evaporators: the distiller presented almost a 50% productivity decrease over 5 days. In contrast, the rinsing process ensured durable distillation performances that, after the first day of testing, stabilized around a limited 15% productivity decrease. Note that to keep the overall desalination process completely off-grid, a photovoltaic panel could be introduced to power a possible rinse pump. A preliminary energy analysis (Supplementary Note 4) indicates that the extension of photovoltaic panel required to power a rinse pump for the three-stage distiller (of the tested size) would be much lower than 1 cm^2 ; namely, less than one-hundredth of the solar-absorbing surface currently required for the distiller. In addition, we note that, regardless of the above rinse, the presence of a pump is required to move the distillate towards the final user.

Discussion

In summary, we present a passive (that is, only driven by non-concentrated solar thermal energy), high-yield, modular, multi-stage and low-cost device that is able to desalinate seawater by complete distillation exploiting the vapour pressure difference across a small gap between two hydrophilic thin layers. The key idea is to use a simple design to reduce the gap between the hydrophilic materials, and hence significantly increase the water vapour permeability. In laboratory and outdoor experiments, we observed that this process is efficiently operated by a thermal power density of less than 1 kW m^{-2} and at a maximum temperature of $<65^\circ \text{C}$. Different methodologies for separating the two hydrophilic layers in each distillation stage were designed and experimentally tested. Furthermore, the desalination performances of the devices with various numbers of distillation stages were assessed to evaluate the modular design efficiency. The device with the best performance provides a specific mass flux of complete distillate up to almost $31 \text{ m}^{-2} \text{ h}^{-1}$ in a 10-stage configuration under laboratory conditions,

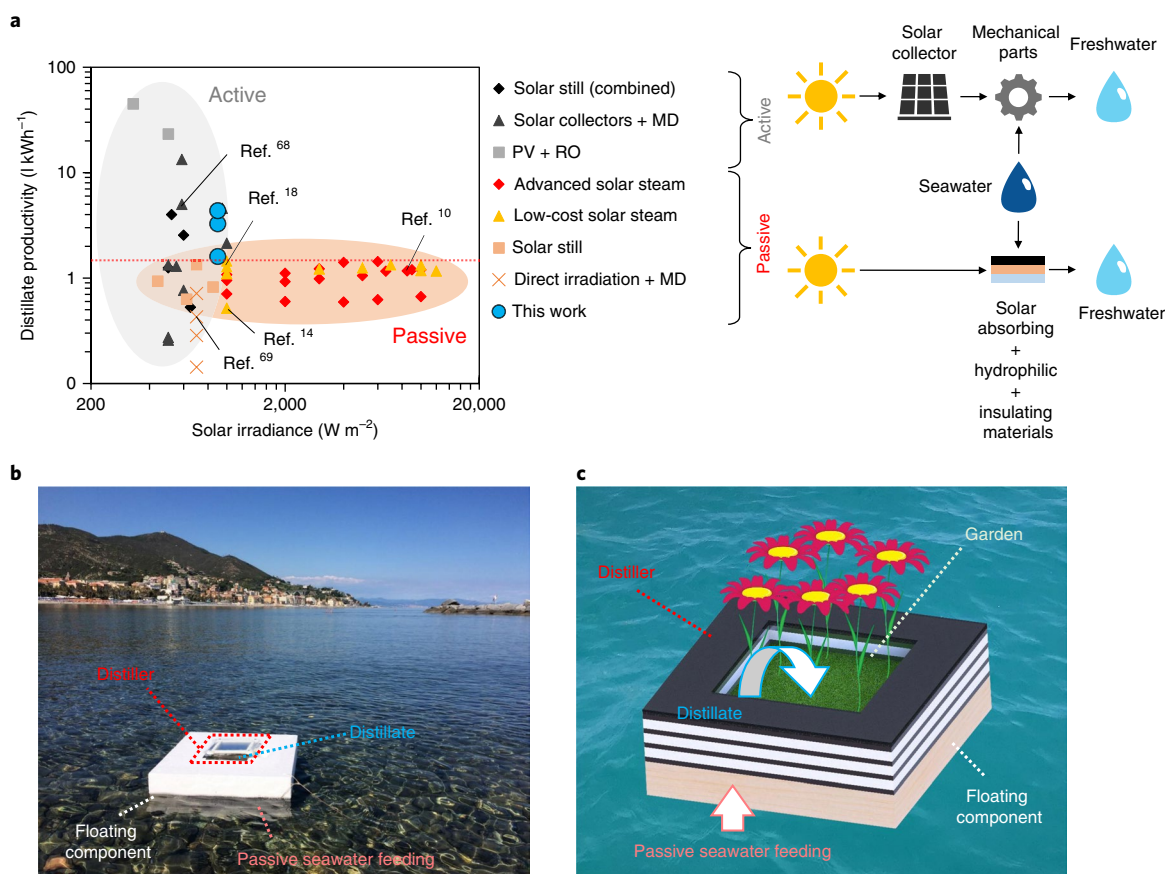


Fig. 4 | Comparison of the modular passive distiller with other solar desalination technologies, and its possible application. **a**, Comparison between the energy desalination performances (that is, litres of distilled water produced per kWh of solar energy input) of active and passive solar desalination technologies from the literature. Unlike active devices that include mechanical moving parts, the working principle of passive technologies only relies on combinations of solar-absorbing hydrophilic layers and thermally insulating materials. Technologies based on complete distillation, membrane distillation (MD), and reverse osmosis (RO) coupled with photovoltaics (PV) processes are depicted. Black rhombi indicate solar stills combined with active components. The performances of the distiller discussed in this work are represented by blue dots. A complete list of the results reported in this graph is given in Supplementary Table 3. The highlighted results refer to the works of Moudjeber et al.⁶⁸, Liu et al.¹⁸, Ghasemi et al.¹⁰, Dongare et al.⁶⁹ and Ni et al.¹⁴. The red dashed line represents the thermodynamic limit of single-stage distillers under one sun (complete distillation; 1.47 l kWh⁻¹). **b**, Floating installation of the modular distiller, which could be employed in emergency conditions (for example, splashdowns, floods or tsunamis). A larger amount of drinkable water could be achieved by mosaic-like arrangements of small-sized distillers, each one fed by separated hydrophilic strips, to limit and optimize the water transport distance by capillarity. **c**, Possible configuration of the floating desalination device tested in this work, where the distilled water could be used to sustain floating gardens.

whereas theoretical modelling shows a potential up to 61 m² h⁻¹. Such theoretical potential could be experimentally approached by increasing the thermal insulation between distillation stages and the ambient surroundings, improving the salt removal process, or optimizing the thickness, material and assembly of hydrophilic layers and membranes. Clearly, recent advances in the materials and technologies used in traditional membrane distillation systems could be beneficial for improving the performances and industrial scalability of our passive desalination device^{35–38}. For example, membrane fouling³¹ could be mitigated by the use of materials, treatments and strategies with anti-fouling capabilities^{39–42}, and recent hydrophilic materials with anti-clogging properties specifically devised for solar desalination could reduce fouling and prevent adhesion and accumulation of salt particles in the evaporators (further discussions are provided in Supplementary Note 5)^{43–45}. Overall, the passive distillers discussed in this work show energy performances that are up to four times higher than those of state-of-the-art passive solar desalination systems for complete distillation^{10–15,18} and, although not within the scope of this work, even show similar performance compared with some of the active desalination technologies (see Fig. 4a and Supplementary Tables 3 and 4).

The low-cost, multi-stage and passive working principle of the distiller introduced in this work may be particularly suitable to provide inexpensive distilled water in cases of emergency conditions. For example, in the floating installation tested by the experiments (see Fig. 4b), seawater is supplied to the modular distiller by capillary action, then desalinated under direct solar energy. These characteristics would be ideal to provide drinkable water after splashdowns, floods or tsunamis, where off-grid operating conditions are forced temporarily by the emergency condition. The distilled water could also be used to sustain permanently floating gardens (see Fig. 4c) for food production and/or CO₂ sequestration. It is worth noting that the floating configuration of the distiller improved its performance because of the reduced and stable temperature of the heat sink realized by the sea. Non-floating configurations of the distiller may also provide freshwater to coastal areas under water stress conditions; for example, the surface of decommissioned off-shore oil rigs⁴⁶ could host up-scaled versions of the distiller with no additional environmental impact. Note that the modular distiller may be also suitable for treating different feed water types in non-coastal areas; for instance, mining, municipal or industrial wastewater^{47–49}.

Methods

Experimental materials and methods. The experimental setup used for evaluating the desalination performance of the passive distiller under laboratory conditions is depicted in Supplementary Fig. 5. To mimic the process of solar energy collection, a planar electrical resistor made of enamelled copper wire with a 0.4 mm diameter was embedded below the selective solar-absorbing layer of the prototype. The electrical resistor was designed to provide a steady heat flux equal to $q = 740 \text{ W m}^{-2}$, which was determined by decreasing the typical peak summer solar irradiation in Torino (approximately 900 W m^{-2}) to account for the solar transmittance of the thermal insulator ($\tau = \sim 0.86$; transparent LLDPE, measured experimentally) and solar absorbance of the selective solar absorber ($\alpha = \sim 0.95$; TiNOX)³⁴. We note that the experimental setup under laboratory conditions mimics realistic operation provided that the resistor delivers the expected absorbed energy, while both radiative and convective heat losses are also accounted for.

We explored three options for achieving small separation of the two liquid phases held in the hydrophilic layers in each stage of our distiller. The first was to maintain an air gap using a ~ 1 -mm-thick polypropylene spacer with 0.62 porosity (Supplementary Fig. 3b). For the second and third options, we used hydrophobic PTFE membranes with a thickness of 0.15 mm and a pore size of either 0.1 or 3.0 μm (Supplementary Fig. 3c). The pore size of hydrophobic membranes is critical for avoiding contamination between the liquid phases that they separate (that is, the smaller the pore size, the higher the liquid entry pressure; thus, the lower the contamination issues⁵⁰). However, because our system operates at ambient pressure, even large pore sizes are not of particular concern for accidental distillate contamination. In fact, the liquid entry pressures of the membranes with pore sizes of 0.1 and 3.0 μm are 7.9 and 0.25 bar, respectively. The value of 0.25 bar could possibly lead to faster membrane wetting; however, no salt contamination was observed in the distillate produced during the experiments.

The testing facilities adopted under laboratory conditions consisted of a laptop for data storage and analysis, a data acquisition board (NI-9213 module for the data acquisition DAQ board; National Instruments), a power supply to provide electrical power to the planar electric resistor mimicking field-test conditions, analogic (RS 110; Hanna Instruments; accuracy $\pm 0.2\%$) and digital (HI 96801; Hanna Instruments; accuracy $\pm 0.2\%$) refractometers, a precision scale (Kern PCB 1000-2; 0.01 g resolution), the distiller prototype and inlet/outlet water basins (100 ml capacity; room temperature). Three thermocouples (RS Pro; K-type) connected to the data acquisition DAQ board recorded the ambient temperature, average temperature of the spectrally selective solar absorber (evaporator in the first stage) and average temperature of the heat sink (condenser in the last stage). The two averaged temperatures allow the estimate of the overall temperature drop across the N -stage distiller. The laboratory precision scale was used to monitor the mass change over time of the distilled water basin, and thus to compute the distillate specific mass flux generated by the distiller. Refractometers were adopted to measure the salt concentration in the saltwater basin as well as to verify the quality of distillate during operation.

The outdoor tests on the rooftop of the Department of Energy at Politecnico di Torino (Torino, Italy) were carried out on 16 and 17 March 2017. Without losing generality, only the evaporator–condenser interface design incorporating a hydrophobic membrane with a pore size of 3 μm was tested. The experimental setups adopted during these outdoor tests (see Supplementary Fig. 8) were similar to those used in the laboratory tests, except that the power supply was no longer needed and a pyranometer (LP Pyra 08 BL; Delta OHM) was used to monitor the solar irradiance. In the tests on the rooftop, the distillate flow rates and their uncertainties were computed from approximately 13:00 to 14:30. The outdoor tests in the sea were carried out in Varazze, Italy on 17 May 2017 (see Supplementary Fig. 10), and the distillate flow rate was computed by considering the cumulative distillate production from approximately 11:30 to 15:30.

The permeability of the hydrophobic membranes was measured via a diffusion cell (15 mm Side-Bi-Side Cell; PermeGear; 7 ml volume). In this setup, as schematically represented in Supplementary Fig. 13, two aqueous salt solutions with different salt concentrations were separated by the clamped hydrophobic membrane. Owing to the concentration gradient, the generated osmotic pressure promotes water flux through the membrane. Freshwater flows through the membrane to the cell containing the solution with higher salinity, and the mass flow rate (thus, the membrane permeability) can be evaluated by monitoring the water level in a graduated column⁵¹. Both sides of the diffusion cells are agitated by stir bars to avoid possible concentration polarization issues at the membrane interfaces.

Theoretical model. The driving force for the N -stage distillation process is the difference in water vapour pressure between the evaporating (E) and condensing (C) hydrophilic layers due to both temperature and salinity differences through the air gap or the hydrophobic membrane^{50,52}. The vapour pressure gradient can be computed using Raoult's law as follows:

$$\Delta p_v = a(Y_E)p_v(T_E) - a(Y_C)p_v(T_C) \quad (1)$$

where a denotes the activity of water, Y_E and Y_C are the mass fractions ($Y = m_{\text{salt}}/m_{\text{solution}}$) of salt in the feed and distilled solution, respectively, p_v is the

water vapour pressure, and T_E and T_C are the temperatures of the feed and distilled solutions, respectively⁵³. Under ideal conditions, the activity of an NaCl aqueous solution can be estimated as:

$$a = \frac{M_{\text{NaCl}}(1-Y)}{M_{\text{NaCl}}(1-Y) + N_{\text{ion}}M_{\text{H}_2\text{O}}} \quad (2)$$

where $N_{\text{ion}} = 2$ for NaCl, and M_{NaCl} and $M_{\text{H}_2\text{O}}$ are the molar masses in grams per mole of sodium chloride and water, respectively. The feed water processed in the experiments has a salinity of 35 g l^{-1} ($Y_E = 0.035$), which is typical for seawater; therefore, equation (2) predicts $a(Y_E) = \sim 0.98$. The activity of distilled water is clearly 1. The vapour pressure can be evaluated via Antoine's semi-empirical correlation:

$$\log[p_v] = A - \frac{B}{C+T} \quad (3)$$

where p_v is intended in mmHg and T in Celsius, and A , B and C are material-specific constants, in this case equal to 8.07, 1,730.63 and 233.42, respectively⁵⁴. In Fig. 1d, the vapour pressure is plotted as a function of water salinity and temperature, according to equations (1)–(3). The operating conditions of an illustrative single stage of the distiller are reported, where saltwater (35 g l^{-1} salinity) in the evaporator and distilled water in the condenser have temperatures of 55 and 45 °C, respectively. It is worth pointing out that, for the sake of illustration, we are neglecting the thermal resistances of the hydrophilic layers. Under these conditions, Fig. 1d illustrates both Δp_v during operating conditions ($\Delta T = 10$ °C) and the minimum temperature drop (ΔT_{min}) needed to carry out the distillation process.

The produced specific mass flow rate of distillate (J , $\text{kg s}^{-1} \text{m}^{-2}$) is derived combining the Maxwell–Stefan and dusty-gas models^{55–57}. The Maxwell–Stefan model considers the external driving force (which includes the concentration effect; namely, the chemical potential) and the molecular diffusion (which describes the interaction between gas molecules). The dusty-gas model takes into account the interaction between gas molecules and the porous matrix (namely, the collision between gas molecules and pore walls) and the viscous flow due to the total pressure gradient across the porous medium. According to the combination of these models, the mass transport through a porous medium can be modelled as:

$$-\frac{x_i}{RT} \frac{d\mu_i}{dz} = \frac{x_i K_v \tau}{\eta_v \epsilon_m D_{iK}} \frac{dP}{dz} + \sum_{j=1}^n \left(\frac{x_j N_i - x_i N_j}{\frac{P \epsilon_m D_{ij}}{RT \tau}} \right) + \frac{N_i}{RT \tau} \quad (4)$$

where x_i is the mole fraction of species i , μ_i is the chemical potential of species i , R is the gas constant ($8.314 \text{ J K}^{-1} \text{ mol}^{-1}$) and T is the absolute temperature. The three terms on the right-hand side of equation (4) consider the viscous flow, molecular diffusion and Knudsen diffusion, respectively. K_v is the viscous permeability coefficient, τ is the tortuosity factor of the membrane, η_v is the dynamic viscosity of the mixture, ϵ_m is the porosity of the membrane, P is the total pressure of the mixture, z is the vertical coordinate and D_{iK} is the Knudsen diffusion coefficient for species i . Furthermore, N_i is the molar flux of species i , and D_{ij} is the diffusion coefficient of species i in species j .

Several assumptions may be considered to simplify equation (4), as extensively discussed by Elimelech and co-workers^{55–57}. First, the ternary mixture (namely, water vapour + nitrogen + oxygen) can be considered as an ideal binary mixture of water vapour and air where, due to the low solubility of air in water, the air molecules trapped in the pores are almost stationary. Consequently, the molar flux of air is zero (namely, $N_a = 0$). In addition, the viscous flow term can be safely neglected in the considered passive device, since there is no total pressure difference across the membrane (unlike typical membrane distillation systems)⁵⁸. Note that, due to the ideal gas assumption, the chemical potential of water vapour (μ_w) is given by the following expression: $\mu_w = \mu_{w,\text{pure}} + RT \ln[x_w]$, where the subscripts w and w_{pure} refer to water and pure water vapour, respectively^{55–57}. Based on these assumptions, and considering a configuration where a membrane (with porosity ϵ_m) of thickness d_m and an air gap (with porosity ϵ_a and $\tau = 1$; see Supplementary Figs. 3b and 12) of thickness d_a are located between the evaporator and condenser in one distiller stage, equation (4) can be respectively integrated within the membrane and air gap, considering as boundary conditions $x_w^E = \frac{a(Y_E)p_v(T_E)}{P}$ when $z = z_E$ (evaporator side), $x_w^0 = \frac{a(Y_0)p_v(T_0)}{P}$ when $z = z_0$ (interface between the membrane and air gap), and $x_w^C = \frac{a(Y_C)p_v(T_C)}{P}$ when $z = z_C$ (condenser side). Of course, $z_0 - z_E = d_m$ and $z_C - z_0 = d_a$. These integrations yield:

$$J = C_1 \ln \left[\frac{1 + \frac{D_{wa}}{D_{wK}} - x_w^0}{1 + \frac{D_{wa}}{D_{wK}} - x_w^E} \right] \quad (5)$$

and:

$$J = \frac{C_1}{C_2} \ln \left[\frac{1-x_w^C}{1-x_w^0} \right] \quad (6)$$

where $J = M_{\text{H}_2\text{O}} N_w$ is the specific mass flow rate of the distillate through the stage, $M_{\text{H}_2\text{O}}$ is the molar mass of water (expressed as kg mol^{-1}), $C_1 = \frac{M_{\text{H}_2\text{O}} P \epsilon_m D_{wa}}{RT d_m}$, $C_2 = \frac{\epsilon_m d_a}{r \epsilon_s d_m}$, P is the total pressure, D_{wa} is the diffusion coefficient of water vapour in air and D_{wk} is the Knudsen diffusion coefficient of water vapour. Thus, with $d_a > 0$, equations (5) and (6) model the following terms, respectively: Knudsen and molecular diffusion within the membrane, and molecular diffusion within the spacer or air gap^{58,59}. Note that it is possible to empirically estimate $PD_{wa} = 1.19 \times 10^{-4} T^{1.75}$ (expressed as $\text{Pa m}^2 \text{s}^{-1}$)⁶⁰. The Knudsen diffusion coefficient is expressed as:

$$D_{wk} = \frac{8r}{3} \sqrt{\frac{RT}{2\pi M_{\text{H}_2\text{O}}}} \quad (7)$$

where r is the average pore radius of the membrane. The correlation between tortuosity and porosity of the membrane is modelled by the Mackie–Meares equation as^{61–63}:

$$\tau = \frac{(2 - \epsilon_m)^2}{\epsilon_m} \quad (8)$$

If $x_w \ll 1$, equations (5) and (6) can be approximated by a first-order Taylor series, with J being linearly dependent on the partial pressure gradient via the permeability coefficient (K) of the gap between the two hydrophilic layers; that is:

$$J = K \Delta p_g \quad (9)$$

where Δp_g is derived from equation (1). When the transition flow dominates, in each stage of the distiller, the overall empirical permeability coefficient reported in equation (9) can then be approximated as a series of contributions from the membrane and spacer permeability^{50,59}, namely:

$$\frac{1}{K} = \frac{1}{\frac{\epsilon_m PD_{wa} M_{\text{H}_2\text{O}}}{p_a \tau RT d_m}} + \frac{1}{\frac{2M_{\text{H}_2\text{O}} \epsilon_m r}{3RT d_m} \sqrt{\frac{8RT}{\pi M_{\text{H}_2\text{O}}}}} + \frac{1}{\frac{\epsilon_s PD_{wa} M_{\text{H}_2\text{O}}}{p_a RT d_a}} \quad (10)$$

where p_a is the arithmetic mean of the air partial pressures in the considered domain. It is worth pointing out that the linearized model in equation (9) and approximate permeability corrected by the p_a/P factor in equation (10) have been successfully applied to numerous membrane distillation experiments in the literature^{59,64,65}, since they typically provide predictions nearly equivalent to the combined Maxwell–Stefan and dusty-gas models (see, for instance, Supplementary Fig. 14). A less crude approximation consists in linearizing only equation (6) (namely, $J \approx \frac{C_1}{C_2} (x_w^0 - x_w^C)$) and using the empirical overall permeability coefficient (namely $x_w^0 - x_w^C \approx \frac{C_2/C_1}{1/(KP)} (x_w^E - x_w^C)$). This linearization can be safely justified by noticing that in the air gap, under the typical moist air conditions of interest here the vapour molar fractions $x_w \ll 1$, which combined with equation (5) yields:

$$J = C_1 \ln \left[\frac{1 + \frac{D_{wa}}{D_{wk}} - x_w^C - \frac{C_2/C_1}{1/(KP)} (x_w^E - x_w^C)}{1 + \frac{D_{wa}}{D_{wk}} - x_w^E} \right] \quad (11)$$

Equation (11) has been adopted in the modelling analyses reported in Fig. 2 and Supplementary Figs. 12 and 14.

Despite there being no consensus in the literature about the exact boundary between the transition (molecular + Knudsen) and pure Knudsen regime, here—following a suggestion in recent work by Elimelech and co-workers⁶⁶—we consider that the transport resistance of membranes with a $0.1 \mu\text{m}$ average pore size ($\text{Kn} > 1$, where Kn denotes the Knudsen number) is dominated by collisions between pore walls and vapour molecules and, thus, only Knudsen transport resistance takes place. In contrast, both molecular and diffusion transport resistances were considered for membranes with a $3.0 \mu\text{m}$ average pore size ($\text{Kn} \ll 1$).

As shown in equation (10), the overall gap thickness of each distiller stage (d_g , which accounts for the air gap, spacer and/or membrane thicknesses) is crucial and strongly affects the permeate flux. To achieve high permeability and thus high mass flux, a balance between minimizing heat transport and maximizing mass transport between the layers should be found^{50,52}. The estimates of the membrane permeability by equation (10) are in good agreement (see Supplementary Fig. 15) with those measured experimentally by the diffusion cell in Supplementary Fig. 13. Note that the measured moderate variation of K with pore size (that is, less

than $\pm 10\%$ in the $0.1\text{--}3.0 \mu\text{m}$ range) agrees with both modelling predictions (see Supplementary Fig. 16) and experimental uncertainties⁵⁰.

In each stage of the distiller, the specific heat flux (q , W m^{-2}) between the evaporating and condensing hydrophilic layers is mainly due to water phase changes and heat transfer by conduction; namely:

$$q = \frac{k_{\text{eff},g}}{d_g} (T_E - T_C) + J \Delta h_{LV} + q_l \quad (12)$$

where $k_{\text{eff},g}$ is the effective thermal conductivity in the gap, including conduction through the air, spacer and/or membrane, T_E and T_C are the temperatures of the feed and permeate solution, respectively, J is the specific mass flow rate of water through the gap, Δh_{LV} is the latent heat of vaporization (in the case of partial distillation²⁵, this term should be substituted by $f \Delta h_{LV}$ where $f < 1$ takes into account the apparent reduced heat of evaporation), and q_l is the specific heat loss through the lateral surface of the stage. An equivalent thermal resistance circuit that schematically represents this one-dimensional thermal model is presented in Supplementary Fig. 17. It is noteworthy to mention that, in our passive device, inlet (saltwater) and outlet (distillate) water fluxes are only driven by capillarity; thus, Reynolds numbers are low ($\ll 1$). Therefore, differently from traditional membrane distillation processes that experience temperature polarization issues⁶⁷, convection does not take place in the feed and permeate channels (that is, hydrophilic layers), and heat transfer is mainly due to conduction. This effect is implicitly included in the adopted model, since Δp_v (equation (1)) is computed considering the temperatures at both membrane (or air gap) surfaces, which are readily available from the series of lumped thermal resistances depicted in Supplementary Fig. 17.

Each 1-mm-thick synthetic microfibre hydrophilic layer was glued with a few drops of silicone adhesive to a 1.3-mm-thick aluminium plate to allow evaporator and condenser assembly in each stage. The global heat transfer coefficient of this assembly (synthetic microfibre + aluminium plate) was experimentally measured as $\sim 250 \text{ W m}^{-2} \text{ K}^{-1}$. Furthermore, the thermal conductivity of the wet synthetic microfibre was estimated as a weighted average between the thermal conductivity of the dry synthetic microfibre ($0.04 \text{ W m}^{-1} \text{ K}^{-1}$) and water ($0.6 \text{ W m}^{-1} \text{ K}^{-1}$), where the quantity of absorbed water can be estimated by comparative weight measurements between dry and wet hydrophilic layers.

Statistical analysis. A sampling period of up to 30 min was used for mass flow rate computations. Experimental measures were performed when a steady self-sustained mass flux of output distillate was achieved, and tests continued for up to four consecutive hours to assess the stability of the distillation process. Steady-state conditions were considered as achieved when the linear fitting of the cumulative mass of produced distillate with time provided a coefficient of determination R^2 larger than or equal to 0.999. The raw data of the experiments are reported in Supplementary Data 1 (distillate mass flow rate) and Supplementary Data 2 (temperatures and solar irradiance).

Standard deviations of measured distillate flow rates were computed from the analysis of the time series of experiments at the steady state. In the plots, error intervals are reported in terms of ± 1 s.d.

The errors in the model predictions were calculated from the uncertainties involved in the measurement of the membrane porosity, convection coefficients and assembly geometry (see Supplementary Table 2). In fact, the non-homogeneous layered structure of the stages generates non-ideal contacts between adjacent layers. Therefore, an additional air gap between membranes and hydrophilic layers is considered in the model.

Data availability

The authors declare that the data supporting the findings of this study are available within the paper and its Supplementary Information files.

Received: 30 November 2017; Accepted: 5 November 2018;

Published online: 14 December 2018

References

- Vörösmarty, C. J., Green, P., Salisbury, J. & Lammers, R. B. Global water resources: vulnerability from climate change and population growth. *Science* **289**, 284–288 (2000).
- Kelley, C. P., Mohtadi, S., Cane, M. A., Seager, R. & Kushnir, Y. Climate change in the Fertile Crescent and implications of the recent Syrian drought. *Proc. Natl Acad. Sci. USA* **112**, 3241–3246 (2015).
- Mekonnen, M. M. & Hoekstra, A. Y. Four billion people facing severe water scarcity. *Sci. Adv.* **2**, e1500323 (2016).
- Amy, G. et al. Membrane-based seawater desalination: present and future prospects. *Desalination* **401**, 16–21 (2017).
- Ziolkowska, J. R. Desalination leaders in the global market—current trends and future perspectives. *Water Sci. Technol. Water Supply* **16**, 563–578 (2016).
- Fasano, M. et al. Interplay between hydrophilicity and surface barriers on water transport in zeolite membranes. *Nat. Commun.* **7**, 12762 (2016).

7. Ahsan, A., Imteaz, M., Rahman, A., Yusuf, B. & Fukuhara, T. Design, fabrication and performance analysis of an improved solar still. *Desalination* **292**, 105–112 (2012).
8. Gleick, P. H. Basic water requirements for human activities: meeting basic needs. *Water Int.* **21**, 83–92 (1996).
9. Service, R. Sunlight-powered purifier could clean water for the impoverished. *Science* <https://doi.org/10.1126/science.aal0699> (2017).
10. Ghasemi, H. et al. Solar steam generation by heat localization. *Nat. Commun.* **5**, 4449 (2014).
11. Huang, X., Yu, Y.-H., de Llergo, O. L., Marquez, S. M. & Cheng, Z. Facile polypyrrole thin film coating on polypropylene membrane for efficient solar-driven interfacial water evaporation. *RSC Adv.* **7**, 9495–9499 (2017).
12. Li, X. et al. Graphene oxide-based efficient and scalable solar desalination under one sun with a confined 2D water path. *Proc. Natl Acad. Sci. USA* **113**, 13953–13958 (2016).
13. Liu, K.-K. et al. Wood-graphene oxide composite for highly efficient solar steam generation and desalination. *ACS Appl. Mater. Interf.* **9**, 7675–7681 (2017).
14. Ni, G. et al. Steam generation under one sun enabled by a floating structure with thermal concentration. *Nat. Energy* **1**, 16126 (2016).
15. Zhou, L. et al. Self-assembly of highly efficient, broadband plasmonic absorbers for solar steam generation. *Sci. Adv.* **2**, e1501227 (2016).
16. Yang, Y. et al. Graphene-based standalone solar energy converter for water desalination and purification. *ACS Nano* **12**, 829–835 (2018).
17. Mauter, M. S. et al. The role of nanotechnology in tackling global water challenges. *Nat. Sustain.* **1**, 166–175 (2018).
18. Liu, Z. et al. Extremely cost-effective and efficient solar vapor generation under nonconcentrated illumination using thermally isolated black paper. *Glob. Chall.* **1**, 1600003 (2017).
19. Elimelech, M. & Phillip, W. A. The future of seawater desalination: energy, technology, and the environment. *Science* **333**, 712–717 (2011).
20. Morciano, M. et al. Efficient steam generation by inexpensive narrow gap evaporation device for solar applications. *Sci. Rep.* **7**, 11970 (2017).
21. Li, T. et al. Scalable and highly efficient mesoporous wood-based solar steam generation device: localized heat, rapid water transport. *Adv. Funct. Mater.* **28**, 1707134 (2018).
22. Shi, Y. et al. A 3D photothermal structure toward improved energy efficiency in solar steam generation. *Joule* **2**, 1171–1186 (2018).
23. Li, X. et al. Enhancement of interfacial solar vapor generation by environmental energy. *Joule* **2**, 1331–1338 (2018).
24. Wang, Y. et al. Improved light-harvesting and thermal management for efficient solar-driven water evaporation using 3D photothermal cones. *J. Mater. Chem. A* **6**, 9874–9881 (2018).
25. Zhao, F. et al. Highly efficient solar vapour generation via hierarchically nanostructured gels. *Nat. Nanotechnol.* **13**, 489–495 (2018).
26. Ohshiro, K., Nosoko, T. & Nagata, T. A compact solar still utilizing hydrophobic poly (tetrafluoroethylene) nets for separating neighboring wicks. *Desalination* **105**, 207–217 (1996).
27. Tanaka, H., Nosoko, T. & Nagata, T. A highly productive basin-type-multiple-effect coupled solar still. *Desalination* **130**, 279–293 (2000).
28. Tanaka, H. & Iishi, K. Experimental study of a vertical single-effect diffusion solar still coupled with a tilted wick still. *Desalination* **402**, 19–24 (2017).
29. Fukuia, K., Nosoko, T., Tanaka, H. & Nagata, T. A new maritime lifesaving multiple-effect solar still design. *Desalination* **160**, 271–283 (2004).
30. UN-Water *World Water Assessment Programme: The United Nations World Water Development Report 4: Managing Water Under Uncertainty and Risk* (UNESCO, 2012).
31. Drioli, E., Ali, A. & Macedonio, F. Membrane distillation: recent developments and perspectives. *Desalination* **356**, 56–84 (2015).
32. Cipollina, A., Di Sparti, M., Tamburini, A. & Micale, G. Development of a membrane distillation module for solar energy seawater desalination. *Chem. Eng. Res. Des.* **90**, 2101–2121 (2012).
33. La Cerva, M. et al. On some issues in the computational modelling of spacer-filled channels for membrane distillation. *Desalination* **411**, 101–111 (2017).
34. *TINOX Titan-Absorber: The Most Efficient Way of Transforming Sunlight into Heat* (ALMECO Group, 2017); <https://go.nature.com/2Dy2WQP>
35. Chen, W. et al. High-flux water desalination with interfacial salt sieving effect in nanoporous carbon composite membranes. *Nat. Nanotech.* **13**, 345–350 (2018).
36. Wang, P. Emerging investigator series: the rise of nano-enabled photothermal materials for water evaporation and clean water production by sunlight. *Environ. Sci. Nano* **5**, 1078–1089 (2018).
37. Yan, K.-K. et al. Superhydrophobic electrospun nanofiber membrane coated by carbon nanotubes network for membrane distillation. *Desalination* **437**, 26–33 (2018).
38. Agbaje, T. A., Al-Gharabli, S., Mavukkandy, M. O., Kujawa, J. & Arafat, H. A. PVDF/magnetite blend membranes for enhanced flux and salt rejection in membrane distillation. *Desalination* **436**, 69–80 (2018).
39. Seo, D. H. et al. Anti-fouling graphene-based membranes for effective water desalination. *Nat. Commun.* **9**, 683 (2018).
40. Qiu, H., Peng, Y., Ge, L., Hernandez, B. V. & Zhu, Z. Pore channel surface modification for enhancing anti-fouling membrane distillation. *Appl. Surf. Sci.* **443**, 217–226 (2018).
41. Jhaveri, J. H. & Murthy, Z. A comprehensive review on anti-fouling nanocomposite membranes for pressure driven membrane separation processes. *Desalination* **379**, 137–154 (2016).
42. Zhao, X. et al. Antifouling membrane surface construction: chemistry plays a critical role. *J. Membr. Sci.* **551**, 145–171 (2018).
43. Kashyap, V. et al. A flexible anti-clogging graphite film for scalable solar desalination by heat localization. *J. Mater. Chem. A* **5**, 15227–15234 (2017).
44. Ni, G. W. et al. A salt-rejecting floating solar still for low-cost desalination. *Energy Environ. Sci.* **11**, 1510–1519 (2018).
45. Xu, W. et al. Flexible and salt resistant Janus absorbers by electrospinning for stable and efficient solar desalination. *Adv. Energy Mater.* **8**, 1702884 (2018).
46. Hamzah, B. International rules on decommissioning of offshore installations: some observations. *Mar. Pol.* **27**, 339–348 (2003).
47. Kezia, K., Lee, J., Weeks, M. & Kentish, S. Direct contact membrane distillation for the concentration of saline dairy effluent. *Water Res.* **81**, 167–177 (2015).
48. Kim, H.-C. et al. Membrane distillation combined with an anaerobic moving bed biofilm reactor for treating municipal wastewater. *Water Res.* **71**, 97–106 (2015).
49. Nathoo, J. & Randall, D. G. Thermodynamic modelling of a membrane distillation crystallisation process for the treatment of mining wastewater. *Water Sci. Technol.* **73**, 557–563 (2016).
50. Alkhubdhiri, A., Darwish, N. & Hilal, N. Membrane distillation: a comprehensive review. *Desalination* **287**, 2–18 (2012).
51. Lee, J., Laoui, T. & Karnik, R. Nanofluidic transport governed by the liquid/vapour interface. *Nat. Nanotech.* **9**, 317–323 (2014).
52. Laganà, F., Barbieri, G. & Drioli, E. Direct contact membrane distillation: modelling and concentration experiments. *J. Membr. Sci.* **166**, 1–11 (2000).
53. Incropera, F. P. & De Witt, D. P. *Fundamentals of Heat and Mass Transfer* (John Wiley & Sons, Hoboken, 1985).
54. Poling, B. E., Prausnitz, J. M. & O'Connell, J. P. *The Properties of Gases and Liquids* Vol. 5 (McGraw-Hill, New York, 2001).
55. Deshmukh, A. & Elimelech, M. Understanding the impact of membrane properties and transport phenomena on the energetic performance of membrane distillation desalination. *J. Membr. Sci.* **539**, 458–474 (2017).
56. Lee, J., Straub, A. P. & Elimelech, M. Vapor-gap membranes for highly selective osmotically driven desalination. *J. Membr. Sci.* **555**, 407–417 (2018).
57. Deshmukh, A. et al. Membrane distillation at the water-energy nexus: limits, opportunities, and challenges. *Energy Environ. Sci.* **11**, 1177–1196 (2018).
58. Phattaranawik, J., Jiraratananon, R. & Fane, A. Effect of pore size distribution and air flux on mass transport in direct contact membrane distillation. *J. Membr. Sci.* **215**, 75–85 (2003).
59. Khayet, M. & Matsuura, T. *Membrane Distillation: Principles and Applications* (Elsevier, Amsterdam, 2011).
60. Yun, Y., Ma, R., Zhang, W., Fane, A. & Li, J. Direct contact membrane distillation mechanism for high concentration NaCl solutions. *Desalination* **188**, 251–262 (2006).
61. Mackie, J. & Meares, P. The diffusion of electrolytes in a cation-exchange resin membrane. I. Theoretical. *Proc. R. Soc. Lond. A* **232**, 498–509 (1955).
62. Mackie, J. & Meares, P. The diffusion of electrolytes in a cation-exchange resin membrane. II. Experimental. *Proc. R. Soc. Lond. A* **232**, 510–518 (1955).
63. Srisurichan, S., Jiraratananon, R. & Fane, A. Mass transfer mechanisms and transport resistances in direct contact membrane distillation process. *J. Membr. Sci.* **277**, 186–194 (2006).
64. Schofield, R., Fane, A., Fell, C. & Macoun, R. Factors affecting flux in membrane distillation. *Desalination* **77**, 279–294 (1990).
65. Lawson, K. W. & Lloyd, D. R. Membrane distillation. *J. Membr. Sci.* **124**, 1–25 (1997).
66. Straub, A. P., Yip, N. Y., Lin, S., Lee, J. & Elimelech, M. Harvesting low-grade heat energy using thermo-osmotic vapour transport through nanoporous membranes. *Nat. Energy* **1**, 16090 (2016).
67. Ali, A., Macedonio, F., Drioli, E., Aljlil, S. & Alharbi, O. Experimental and theoretical evaluation of temperature polarization phenomenon in direct contact membrane distillation. *Chem. Eng. Res. Des.* **91**, 1966–1977 (2013).
68. Moudjebber, D.-E., Ruiz-Aguirre, A., Ugarte-Judge, D., Mahmoudi, H. & Zaragoza, G. Solar desalination by air-gap membrane distillation: a case study from Algeria. *Desalin. Water Treat.* **57**, 22718–22725 (2016).
69. Dongare, P. D. et al. Nanophotonics-enabled solar membrane distillation for off-grid water purification. *Proc. Natl Acad. Sci. USA* **114**, 6936–6941 (2017).

Acknowledgements

The authors are grateful to 'Fondazione CRT—Torino' under the NANOSTEP project ('La Ricerca dei Talenti' call; grant number 911/2015). E.C. acknowledges partial financial support from the Politecnico di Torino through the Starting Grant (grant number 56_RIL16CHE01). The authors also thank M. Bressan and R. Costantino for laboratory support, S. Pezzana (Almec Group) for providing experimental materials, and P. Ornelio and the Marina di Varazze and Lega Navale Varazze institutions for hosting field tests of the floating distiller. In particular, we acknowledge L. Molin Pradel (Marina di Varazze) for generous hospitality. This work was performed under the auspices of the CleanWaterCenter@PoliTo (<http://cleanwater.polito.it/>).

Author contributions

P.A. initially suggested the study of a passive floating panel exploiting materials with high solar absorptance and hydrophobic microporous membranes for seawater desalination. E.C. conceived the ideas of both the thin hydrophilic layers separated by an air gap as a passive distiller unit (membrane-free solution) and the multi-stage gain of freshwater flux. P.A. developed the theoretical model and suggested the rinse strategy. M.M. and

M.F. assembled the prototypes and conducted the computations. M.M. conducted the experiments with the help of F.V. and M.F. E.C. and P.A. supervised the research with the help of M.F. All authors contributed to writing the paper.

Competing interests

The authors declare no competing interests.

Additional information

Supplementary information is available for this paper at <https://doi.org/10.1038/s41893-018-0186-x>.

Reprints and permissions information is available at www.nature.com/reprints.

Correspondence and requests for materials should be addressed to E.C. or P.A.

Publisher's note: Springer Nature remains neutral with regard to jurisdictional claims in published maps and institutional affiliations.

© The Author(s), under exclusive licence to Springer Nature Limited 2018